Atmospheric Environment 358 (2025) 121340

Contents lists available at ScienceDirect

Atmospheric Environment

journal homepage: www.elsevier.com/locate/atmosenv

Global health impacts of PAHs based on high-resolution modeling by dynamic simulation and relative emission downscaling

Zichen Wu [a,b,c], Xueshun Chen [a,b,c,*], Yuanlin Wang [d,a], Wenyi Yang [e], Yang Wang [c,f], Zhe Wang [a,b,c], Huansheng Chen [a,b,c], Lianfang Wei [g], Wending Wang [a,b,c], Huiyun Du [a,b,c], Zhuoran Wang [a,b,c], Ying Wei [h], Xiao Tang [a,b,c], Jie Li [a,b,c], Lin Wu [a,b,c], Zifa Wang [a,b,c,**]

[a] State Key Laboratory of Atmospheric Boundary Layer Physics and Atmospheric Chemistry, Institute of Atmospheric Physics, Chinese Academy of Sciences, Beijing, 100029, China
[b] State Key Laboratory of Atmospheric Environment and Extreme Meteorology, Institute of Atmospheric Physics, Chinese Academy of Sciences, Beijing, 100029, China
[c] University of Chinese Academy of Sciences, Beijing, 100049, China
[d] UK Centre for Ecology & Hydrology Edinburgh, Bush Estate, Penicuik, EH26 0QB, UK
[e] Chinese Academy of Environmental Planning, Beijing, 100041, China
[f] Research Center for Eco-Environmental Sciences, Chinese Academy of Sciences, Beijing, 100085, China
[g] Chinese Research Academy of Environmental Sciences, Beijing, 100012, China
[h] Institute of Urban Meteorology, China Meteorology Administration, Beijing, 100089, China

HIGHLIGHTS

- The 0.1° × 0.1° simulation by downscaling improves the global BaP accuracy.
- Health risk due to BaP at 0.1° × 0.1° resolution has increased by over 50 %.
- Health risk due to BaP is significantly higher in winter than in other seasons.
- Health risk due to BaP is larger for children and young adults than for other groups.

ARTICLE INFO

Keywords:
Health risks
Polycyclic aromatic hydrocarbons
High-resolution
Downscale
Dynamic simulation

ABSTRACT

Polycyclic aromatic hydrocarbons (PAHs) are one of the highly toxic pollutants that require strict control. High-resolution distribution of PAHs is crucial for accurately quantifying their population exposure levels. However, due to the high computational cost, few models applying the dynamical approach could simulate global PAHs to evaluate health effects with resolution down to 1–10 km. This study simulated the global distribution of PAHs by combining the IAP-AACM model with a nonlinear downscaling method based on relative anthropogenic emissions and observations. A global high-resolution (0.1° × 0.1°, ~10 km in middle latitudes) dataset of Benzo[a] pyrene (BaP, the most representative PAHs) in 2013 and 2018 is generated to support exposure studies. The 0.1° × 0.1° results are comparable to the nested simulation and have better consistency with observations than that of the 1° × 1° simulation. The 0.1° × 0.1° estimation shows significantly higher population-weighted total incremental lifetime cancer risks (PTILCR), with an increase larger than 50 %, compared to the 1° × 1° simulation. The PTILCR is greatly higher in winter than in other seasons and it is larger for children and young adults than for adolescents and seniors. The study has significant implications for the reliable assessment of global health risks of PAHs and the development of scientific management strategies for different age groups.

* Corresponding author. Institute of Atmospheric Physics, Chinese Academy of Sciences, Beijing, 100029, China.
** Corresponding author. Institute of Atmospheric Physics, Chinese Academy of Sciences, Beijing, 100029, China.
E-mail addresses: chenxsh@mail.iap.ac.cn (X. Chen), zifawang@mail.iap.ac.cn (Z. Wang).

https://doi.org/10.1016/j.atmosenv.2025.121340
Received 2 February 2025; Received in revised form 27 May 2025; Accepted 7 June 2025
Available online 8 June 2025

1. Introduction

Polycyclic aromatic hydrocarbons (PAHs) are a kind of persistent organic pollutants (POPs), mainly produced by anthropogenic activities such as organic residues and incomplete combustion of fuels (Chang et al., 2006; Liao and Yu, 2020). Different from many other POPs, PAHs are by-products of combustion, i.e., they are not intentionally produced (Friedman et al., 2014). In addition, PAHs can be produced by natural processes, such as volcanic eruptions and wildfires (Fu et al., 2023). Exposure to PAH-containing environments increases the risk of cancer in humans (Boström et al., 2002; Xia et al., 2013), and it can enter the human body through inhalation and dermal contact routes (Ma et al., 2020). PAHs have been classified as human mutagens and carcinogens by the World Health Organization (WHO) due to their different toxicity levels (World Health Organization, 2000; Ting et al., 2023). The United States Environmental Protection Agency (USEPA) has identified 16 PAHs as priority pollutants (Li et al., 2023). Among them, benzo[a] pyrene (BaP), the first chemical carcinogen to be discovered (Ravindra et al., 2008), is often studied as a representative substance of PAHs (Cao et al., 2022; Zhang et al., 2011; Zhu et al., 2015). Thus, understanding the spatial and temporal distribution characteristics of BaP in the atmosphere is essential for assessing its impact on the environment and human health.

The environmental persistence and semi-volatility of PAHs allow them to be transported over long distances (Marusenko et al., 2011; Zhang and Chen, 2017). The health risks assessment based on a long-term and broad regional analysis of atmospheric PAHs through monitoring is costly and technically limited. Modeling is an effective tool for representing the chemical and physical processes of PAHs, and has been widely used to investigate their spatial and temporal distribution in the atmosphere. (Byun and Schere, 2006). At present, several modeling studies of PAHs at the global scale have been reported, with resolutions ranging from $4.5^\circ \times 4.5^\circ$ to $1^\circ \times 1^\circ$ (Lammel et al., 2009, 2015; Lou et al., 2023; Octaviani et al., 2019; Shrivastava et al., 2017). Models with these resolutions can only provide averaged concentrations within grids of 100×100 km to 500×500 km, which cannot capture detailed spatial variation, especially the hotspots in heavily polluted areas (Wang et al., 2014), and thus are insufficient for investigating the health risks of PAHs (Shen et al., 2014). Along with the increase in resolution ($0.1^\circ \times 0.1^\circ$), the number of grids will increase exponentially, greatly increasing the computation costs (Dinkelacker et al., 2023; Rivera et al., 2022). For this reason, it remains challenging for global chemical transport models to perform simulations at high resolutions ($\leq$10 km).

Downscaling based on emission and meteorological factors is an efficient method to derive a high-resolution distribution of PAHs. For example, Shen et al. (2014) established a method to downscale the PAHs distribution from $1.875^\circ \times 1.895^\circ$ to $0.1^\circ \times 0.1^\circ$. Shrivastava et al. (2017) and Lou et al. (2023) also applied this method to enhance the data resolution from $1.9^\circ \times 2.5^\circ$ to $0.1^\circ \times 0.1^\circ$, finding that high-resolution data could increase the BaP concentration by about a factor of two in some areas, thereby increasing the associated health risks. The above studies demonstrate that model resolution significantly impacts simulated concentrations, with higher resolution enhancing the model's ability to capture detailed spatial variability, resulting in better agreement between simulations and observed values. However, few studies have compared the downscaled PAHs concentrations with high-resolution dynamical simulations for data validation, and the differences in global health risks based on low and high resolution have yet not been quantified. In addition, the uncertainties in the global high-resolution estimation of the health risks of PAH remain to be further addressed although some studies using Monte Carlo simulations have investigated the sensitivity of parameters such as inhalation rate, body weight, and cancer slope factor (Xia et al., 2013; Zhang et al., 2016, 2023). In this paper, we assessed the global health risks of BaP based on a high-resolution simulation. The results are helpful to view the global distribution of BaP and evaluate the health risks induced by PAHs. The structure of this paper is as follows: Section 2 describes the global model, the downscaling approach, and the health risk assessment method. Section 3 shows the downscaling results, the impact of resolution on health risks due to PAHs, and an uncertainty analysis. Section 4 summarizes the main conclusions.

2. Method

2.1. Description of model

The global atmospheric chemical transport model is the Atmospheric Aerosol and Chemistry Model developed by the Institute of Atmospheric Physics, Chinese Academy of Sciences (IAP-AACM) (Wei et al., 2019). The model uses nesting method across multi-domain to simulate atmospheric processes from global to regional scales. The model has been widely used to investigate dust transport (Li et al., 2012), regional ozone pollution and haze formation (Du et al., 2019; Wang et al., 2001), global transport of mercury (Chen et al., 2015), new particle formation (Chen et al., 2019), and the global distribution of particle number concentration (Chen et al., 2021).

Recently, we incorporated several chemical and physical processes to simulate PAHs in the IAP-AACM. The processes include: (1) Gas-particle partitioning, adsorption onto black carbon (BC) and absorption into aerosol organic matter (OM), (2) Gaseous-phase reactions, the reactions of gas-phase PAHs with hydroxyl radical (OH), nitrate radical (NO_3), and ozone (O_3), (3) Heterogeneous reaction with O_3 using a detailed parameterization considering temperature and humidity developed by Mu et al. (2018), (4) Air-soil exchange, using parameters determined in Jury et al. (1983) and Strand and Hov. (1996), and (5) Dry and wet deposition. The detailed model description can be found in Text S1.

In this study, we use nested domains to simulate the distribution of BaP in 2013 and 2018. Each simulation has a one-month spin-up to minimize the influence of initial conditions. The global domain is configured with a horizontal resolution of $1^\circ \times 1^\circ$ to combine the downscaling technique to generate high-resolution datasets ($0.1^\circ \times 0.1^\circ$). The nested domains are focused on eastern China and Central Europe with a horizontal resolution of $0.11^\circ \times 0.11^\circ$, which is set to verify the dataset from the downscaling method. The emission inventory of PAHs was derived from the Emissions Database for Global Atmospheric Research (EDGAR, Crippa et al., 2020, available from https://edgar.jrc.ec.europa.eu/dataset_pop60#sources, last access: May 10, 2024) with a resolution of $0.1^\circ \times 0.1^\circ$, which includes sectors such as industry, transportation, energy for buildings, agriculture, and power. To match the grid of the IAP-AACM, we re-gridded the emission inventory to $1^\circ \times 1^\circ$ and $0.11^\circ \times 0.11^\circ$. The meteorological field input to the IAP-AACM is simulated by the global version of the Weather Research and Forecasting Model (GWRF, version 3.7.1, Skamarock et al., 2008; Zhang et al., 2012). The GWRF initial conditions were produced by Final Analysis data (FNL) from the National Centers for Environmental Prediction (NCEP).

2.2. Description of downscaling methods

Anthropogenic emissions are a major source of PAHs, so we used a nonlinear downscaling method based on relative anthropogenic emissions (RAEs). This method assumes that the subgrid spatial distribution of BaP concentrations is associated with the underlying distribution of emission (Kohl et al., 2023; Wang et al., 2014). It should be noted that this method implicitly incorporates the effect of mixing within the coarse grid by fitting with observation data. Compared to the method used by Shen et al. (2014), the influence of meteorological factors would be underestimated by the method in this study. However, considering that the monthly and annual mean concentration is less affected by the variation of meteorological conditions than the hourly concentration,

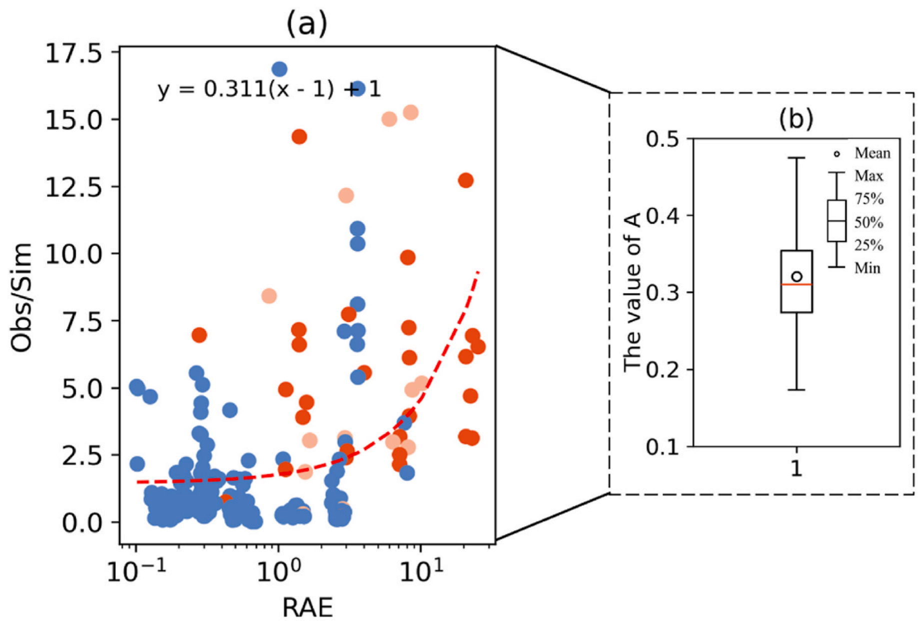

Fig. 1. Scatterplot of (a) relative anthropogenic emission (RAE) versus observations/simulations (Europe: blue; China: red; Japan: pink). The red line represents the fitted curve through the point (1,1). (b) Box plot of the distribution of fitting parameters A. (For interpretation of the references to colour in this figure legend, the reader is referred to the Web version of this article.)

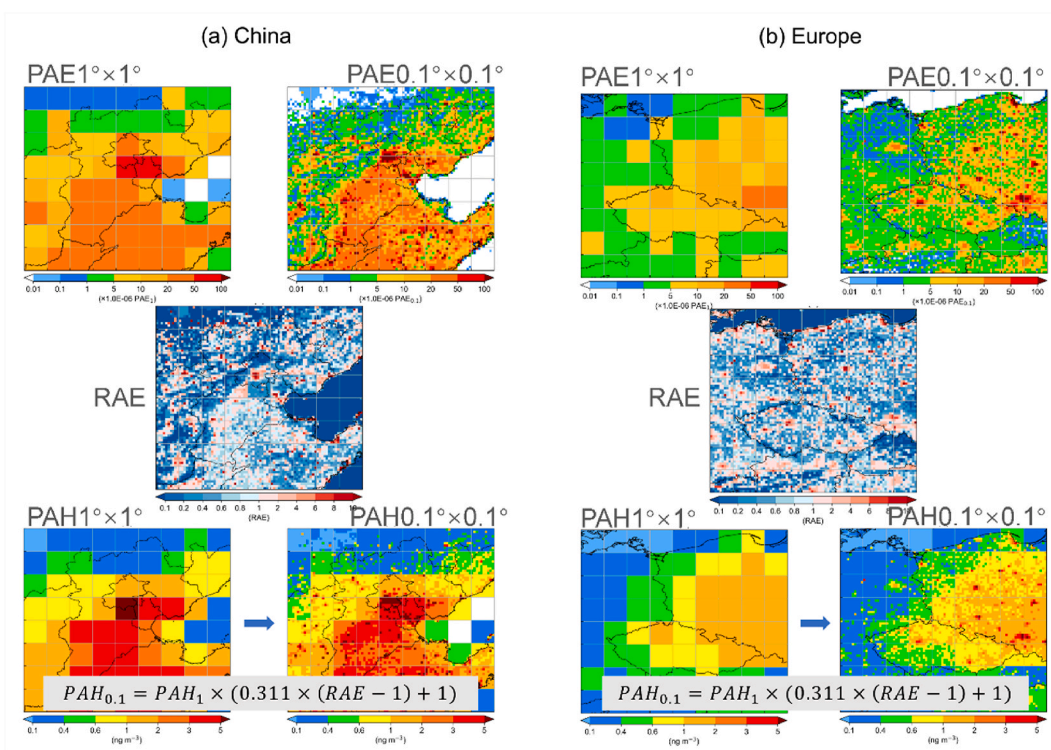

Fig. 2. Illustration of the downscaling process using anthropogenic emissions of PAHs from the EDGAR inventory, using (a) the Beijing-Tianjin-Hebei region (China) and (b) the Czech Republic (Europe) as examples. Relative anthropogenic emissions (middle row) are derived from primary anthropogenic emissions of 1° × 1° and 0.1° × 0.1° (upper row). Results from model resolution (1° × 1°) to 0.1° × 0.1° horizontal resolution (bottom row) are obtained from RAE and Eq. (2). It should be noted that the average RAE in each low-resolution grid box (shown in gray) is equal to 1, ensuring that the mean PAH concentrations in each grid box remain consistent.

the method can be used to generate the high-resolution simulations.

The original resolution of the EDGAR inventory (0.1° × 0.1°) is finer than the resolution of the global simulation (1° × 1°). Specifically, BaP concentrations within the coarse grid were redistributed based on relative emissions, which are defined as the differences in emissions between fine and coarse grids. Key parameters for this redistribution

Table 1
The parameters used in Eq. (3)-Eq. (4) for different groups[a] (lognormal distribution with geometric mean and geometric stand deviation: LN (gm, gsd)).

Parameter	Children (0–6)	Adolescents (7–17)	Young (18–44)	Middle-aged (45–59)	Older (60–79)	The Oldest (> 80)
IR	LN (5.8,1.2)	LN (13.1,1.3)	LN (16.7,1.1)	LN (16.7,1.1)	LN (13.8,1.2)	LN (12.0,1.1)
BW	LN (10.7,1.2)	LN (40.3,1.4)	LN (61.9,1.2)	LN (63.5,1.2)	LN (60.3,1.2)	LN (55.5,1.2)
ED	6	11	27	15	10	5
SA	LN (1050,1.3)	LN (1600,1.4)	LN (2000,1.1)	LN (2000,1.1)	LN (2000,1.2)	LN (1800,1.2)
SFO_{inh}[b]	3.14	3.14	3.14	3.14	3.14	3.14
SFO_{der}[b]	37.47	37.47	37.47	37.47	37.47	37.47

[a] Adapted from Duan et al. (2015); Duan et al. (2016).
[b] Adapted from Hussain et al. (1998).

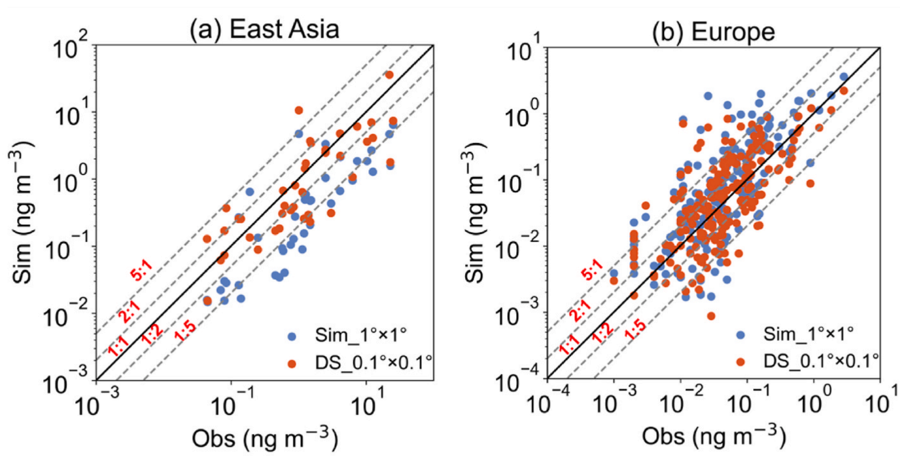

Fig. 3. Comparison of annual mean concentrations of BaP at 1° × 1° resolution (blue) and 0.1° × 0.1° resolution (red) with observations in 2013 in (a) East Asia and (b) Europe. The black line shows a ratio of 1 : 1 and the dashed gray lines from top to bottom show ratios of 5 : 1, 2 : 1, 1 : 2, and 1 : 5, respectively. (For interpretation of the references to colour in this figure legend, the reader is referred to the Web version of this article.)

were derived from observational data, enabling the construction of a high-resolution global distribution of BaP concentrations.

Fig. 2 illustrates the above downscaling process of how to obtain the PAHs dataset at 0.1° × 0.1° horizontal resolution in detail, using the example over the areas in Beijing-Tianjin-Hebei (in China) and Czech Republic (in Europe). We calculated RAEs, i.e., local anthropogenic emissions in the fine grid relative to the averaged emissions of all fine grids within the coarse grid:

$$RAE = PAE_{0.1} / PAE_1 \tag{1}$$

Where $PAE_{0.1}$ is the original anthropogenic emission from the EDGAR inventory (0.1° × 0.1°). PAE_1 is the emission inventory re-gridded to match the IAP-AACM resolution (1° × 1°).

After calculating the *RAE* values, we obtain the nonlinear fitting relationship between the ratios of observations/simulations and *RAE* values (shown in Fig. 1). Nonlinearity arises because the distribution of PAHs in the atmosphere is influenced not only by emissions but also by complex physicochemical processes, such as air-soil exchange and gas-particle partitioning. These processes lead to a nonlinear relationship between the concentrations of PAHs and their emissions. These considerations are implied in adjustments using observations. In the downscaling, the concentration can be greater or less than that in the 1° × 1° simulation depending on whether the value of RAE is greater than or less than 1.

We selected 230 observational datasets from Europe, China, and Japan. For the simulated concentrations, we select the values in the grids where observation sites are located at 1° × 1° resolution. Then, we carry out fitting through the point (1, 1), and the expression obtained is $y = A \times (x - 1) + 1$. The fitting curve is shown as the red curve in Fig. 1a. Where x represents *RAE* and y represents observation/simulation at low resolution. *A* is the fitting parameter, which represents the degree of influence of the change of RAEs on the observation/simulation. We used this relationship to adjust the PAHs simulations, and then obtained the PAHs concentration by downscaling using the equation as follows:

$$PAH_D = PAH_M \times (0.311 \times (RAE - 1) + 1) \tag{2}$$

Where PAH_M is the simulated concentration of PAHs in the coarse grid at low resolution (before downscaling). PAH_D is the calculated concentration of PAHs in the fine grid at high resolution after downscaling.

The fitting parameters have uncertainties associated with the discontinuity and insufficiency of the observational data. Therefore, we randomly selected 120 observations from the total of 230 as a training dataset and conducted 5000 experiments to obtain different fitting parameters. As shown in Fig. 1b, the range of fitting parameter A is between 0.2 and 0.4 in 88 % of the experiments, and the mean value (0.32) is very close to the fitting value (0.311) from the complete dataset.

In addition, we applied Eq. (2) to the simulation results at the low resolution in 2018 to verify the independence of the downscaling process from the data used for fitting, and showed that fitting parameters can be applied to data points outside the training dataset.

2.3. Observational data

To evaluate the performance of the downscaling approach, we collected the observational data of PAHs in Europe, China, and Japan from publicly available datasets and published papers as follows: (1) European Monitoring and Evaluation Program (EMEP, https://projects.nilu.no/ccc/reports.html, last access: May 10, 2024), this includes monthly and annual averages of BaP concentrations from 2003 to 2021 in Poland, Czech Republic, Germany, and other European countries; (2)

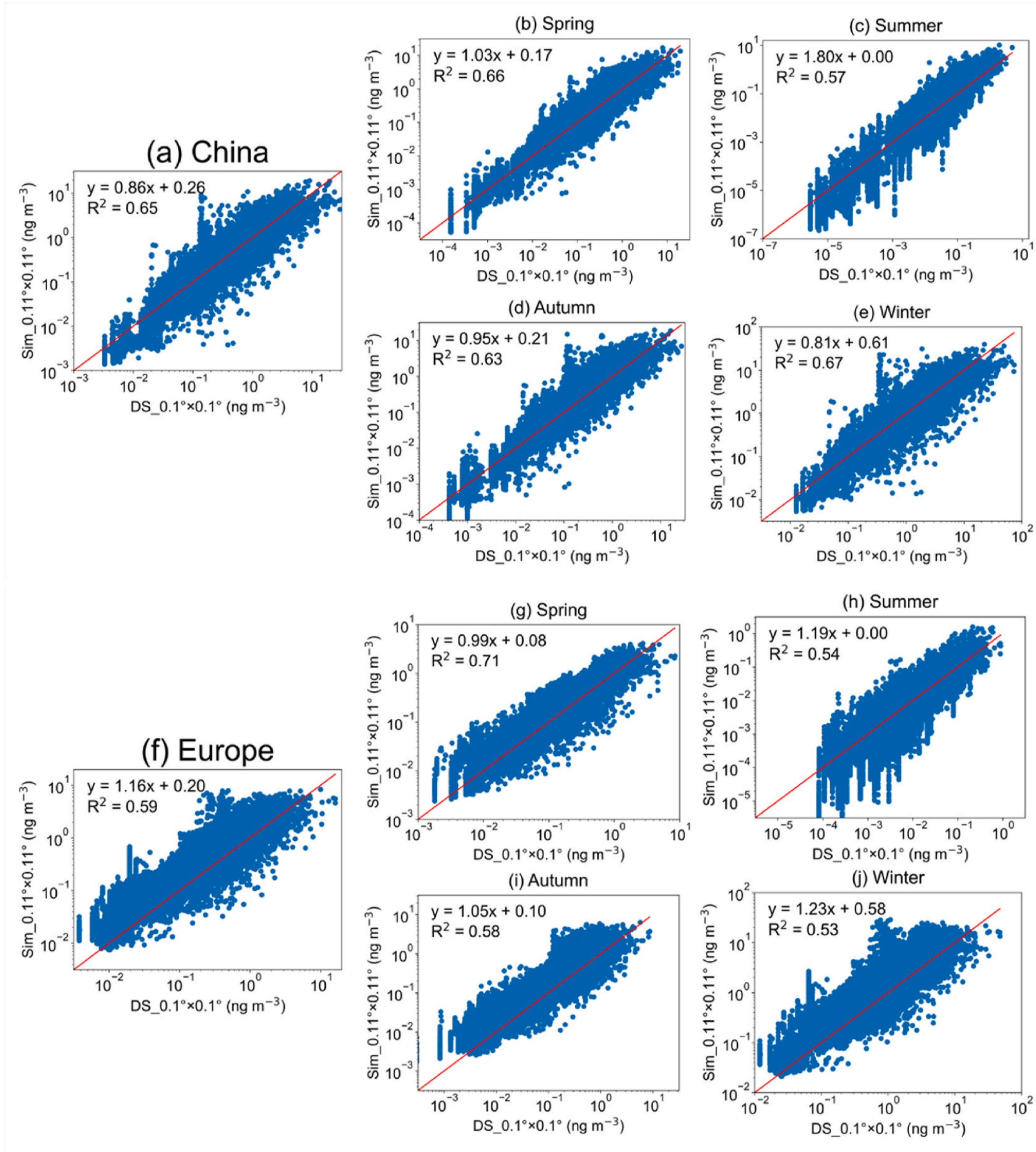

Fig. 4. Spatial correlations between high-resolution simulation (Sim_0.11° × 0.11°) and downscaling result (DS_0.1° × 0.1°) of (a, f) annual and (b-e, g-j) seasonal mean concentrations in (a–e) China and (f–j) Europe (2013).

Chinese Persistent Organic Pollutants (POPs) Soil and Air Monitoring Program Phase II (SAMP-II, Ma et al., 2018) and the reference therein. Due to the limitation of PAHs monitoring technology, the measurements of PAHs in China are very scarce. In addition, most of the observational data are not continuous in time, and we have selected data in years close to the simulation year (2013). These data sources can refer to Wu et al. (2024); (3) Environmental Outlook Station of the National Environmental Research Institute of Japan (NIES, https://tenbou.nies.go.jp/gis/monitor/, last access: May 15, 2024), this includes annual and monthly averages of BaP concentrations in a large number of stations in Japan from 2000 to 2018.

2.4. Health risk assessment

The health risk of PAHs was estimated by the ILCR model proposed by the USEPA (1991). In our evaluation, the population is divided into six age groups, i.e., children (0–6 years old), adolescents (7–17 years old), young adults (18–44 years old), middle-aged adults (45–59 years old), older adults (60–79 years old), and the oldest adults (> 80 years old). The ILCR of BaP through inhalation and dermal contact is calculated as follows:

$$ILCR_{inh} = C \times IR \times EF \times ED \times SFO_{inh} \times cf/AT \times BW \quad (3)$$

$$ILCR_{der} = C \times SA \times ABS \times AF \times EF \times ED \times SFO_{der} \times cf/AT \times BW \quad (4)$$

$$TILCR = ILCR_{der} + ILCR_{inh} \quad (5)$$

where $ILCR_{inh}$ and $ILCR_{der}$ are the ILCR through inhalation and dermal contact, respectively. *TILCR* is the total *ILCR* of exposure through the two pathways. *C* is the concentration of BaP in the atmosphere (ng m^{-3}). We treated inhalation rate (*IR*, m^3 d^{-1}), body weight (*BW*, kg), and skin exposed surface area (*SA*, cm^2), which obeyed lognormal distribution in Eq. (3)-Eq (4) probabilistically. *EF* is the exposure frequency (day $year^{-1}$), which is set as 90 for seasonal exposure and 365 for the whole year exposure. *ED* is the exposure period (year), with values of 6, 11, 27, 15, 10, and 5 for children, adolescents, young adults, middle-aged adults, older adults, and the oldest adults, respectively. SFO_{inh} and SFO_{der} are the carcinogenic slope factor of inhalation and dermal contact

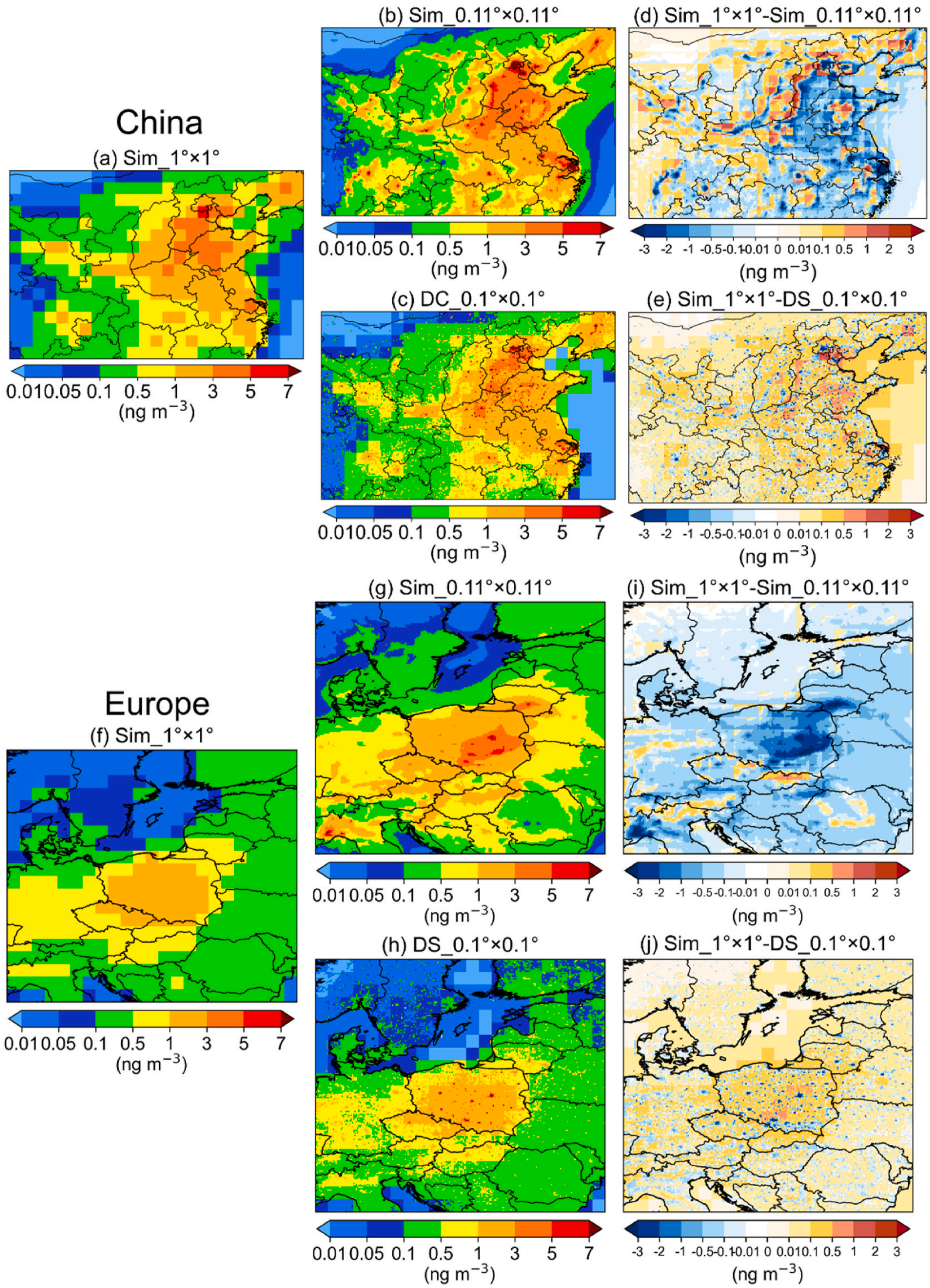

Fig. 5. Spatial distribution of annual mean BaP concentrations at low-resolution ($1^\circ \times 1^\circ$) in (a) eastern China and (f) central Europe in 2013. Comparison of the concentrations at high resolution ($0.11^\circ \times 0.11^\circ$, b/g) and downscaling ($0.1^\circ \times 0.1^\circ$, c/h). The concentration difference between (d/i) high-resolution/(e/j) downscaling results and low-resolution concentrations, positive values indicate that the low-resolution results are greater than the high-resolution/downscaling results, and negative values are the opposite.

respectively (kg day year^{-1}). *cf* is the conversion factor (10^{-6} mg ng^{-1}). *AT* is the average exposure time (25550 days). *ABS* is skin absorption factor (0.13). *AF* is dermal adherence rate (the values are 0.04 for children and adolescent and 0.02 for young adults, middle-aged adults, older adults, and the oldest adults). The values of this parameters are shown in Table 1.

The population data were obtained from LandScan (https://landscan.ornl.gov, last access: June 10, 2024). The original resolution of the data is 1 km × 1 km (at the Equator), and we re-gridded it to $1^\circ \times 1^\circ$ and $0.11^\circ \times 0.11^\circ$ to match the IAP-AACM resolution. When calculating the ILCR, the cancer risk is set to 0 in regions without population. Considering the influence of population distribution (Aunan et al., 2018), we also calculated the population-weighted BaP concentrations (*PC*) for health risk assessment as follows:

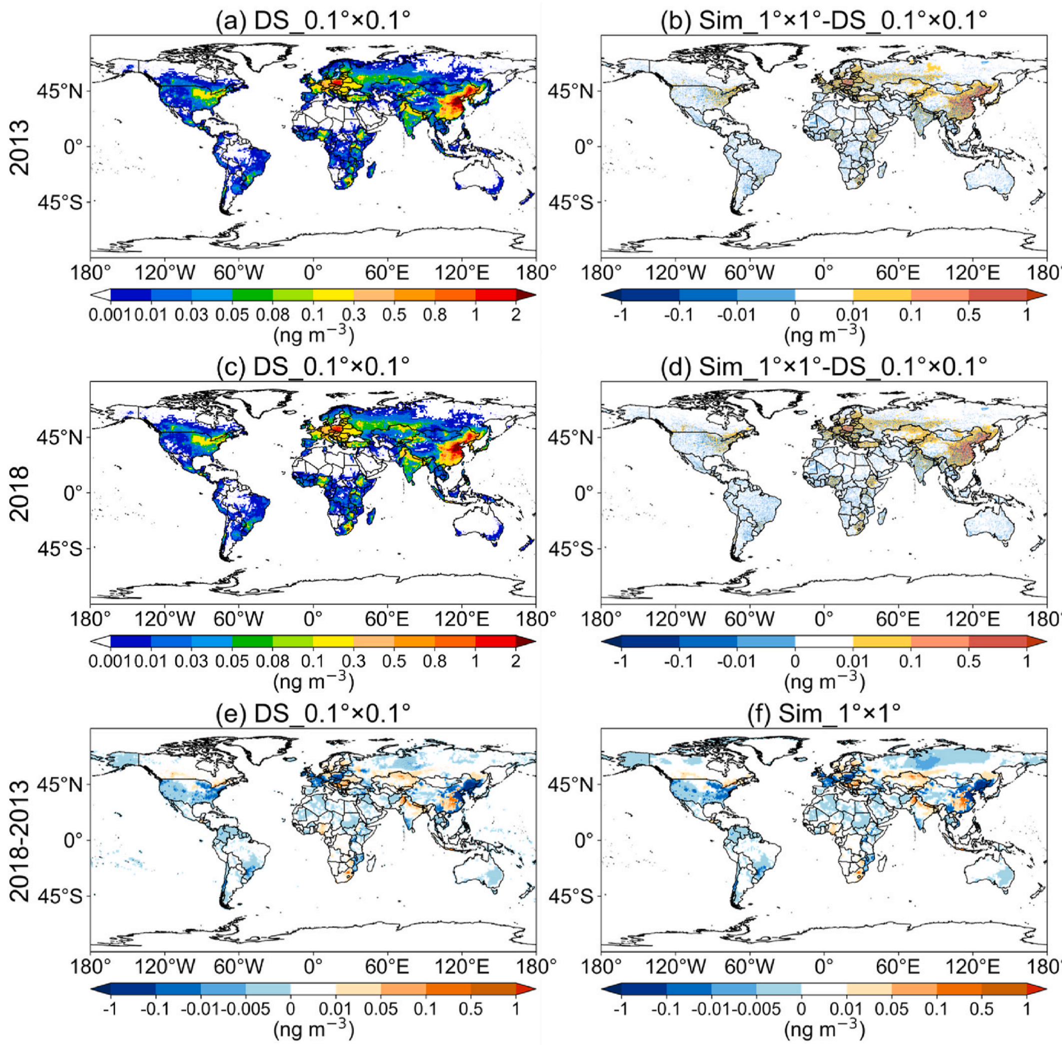

Fig. 6. Spatial distributions of annual mean BaP concentrations (a, c) at 0.1° × 0.1° resolution and the absolute changes between the 1° × 1° resolution and 0.1° × 0.1° resolution in (a, b) 2013 and (c, d) 2018. The absolute (c/e) concentration changes from 2013 to 2018 at (e) 0.1° × 0.1° and (f) 1° × 1° resolution.

$$PC = \sum_i (P_i \times C_i) \Big/ P \tag{6}$$

where C_i is the concentration of BaP for each grid (ng m^{-3}). P_i and P are the population for each grid and total population for the region.

In addition, a Monte Carlo simulation with 10,000 iterations was implemented to investigate the uncertainties of the parameters in the health risk assessment model. Incorporating parameter variability and uncertainty into the health risk assessment provides a more realistic representation of exposure level. The results are presented in the form of probabilities, cumulative probability distributions, and sensitivity analyses, where probability analyses are used to represent the uncertainty of health risks (Xia et al., 2013), and sensitivity analyses are used to assess the relative importance of each input parameter to the output (Chen and Liao, 2006; Fang et al., 2020).

3. Results

3.1. Evaluation of high-resolution data

To evaluate the performance of IAP-AACM, we compared coarse resolution simulations (1° × 1°, before downscaling) and downscaling results (0.1° × 0.1°) with observations in East Asia (Fig. 3a) and Europe (Fig. 3b) in 2013. We find that many simulations are underestimated at some stations in East Asia. This is because of the smoothing effect by averaging high concentration in a coarse-resolution grid. The model can simulate 33 % of the observations within a factor of 2 (PF2) and 76 % of the observed samples within a factor of 5 (PF5) when using 1° × 1° resolution simulation. We further compared the downscaled results with the observational data and found that the underestimation is improved significantly, with PF2 and PF5 increasing to 43 % and 83 %, respectively. Especially in East Asia, the simulations become more closer to the observations, with their $\overline{S/O}$ (geometric mean of the ratio between the simulated and observed values, $\overline{Simulation/Observation}$) changing from 0.43 to 1.12 and NMB (normalized mean bias) decreasing from −0.75 to −0.30. The NMB is also decreased from −0.52 to −0.09 in the European sites. The NMB is −0.39 in the study using downscaling based on emission density, wind speed/direction/frequency (Shrivastava et al., 2017). Our downscaling bias is acceptable although we did not explicitly consider the influence of mixing and transport within the coarse grid.

We further use the seasonal data (Spring: March, April, and May; Summer: June, July, and August; Autumn: September, October, and November; Winter: December, January, and February) to evaluate the downscaling results. The spatial correlations between high-resolution and downscaling results of annual and seasonal mean BaP concentrations in China and Europe are shown in Fig. 4. The downscaling method effectively captures the seasonal variation in BaP concentrations in the atmosphere, providing a reliable foundation for using this approach to

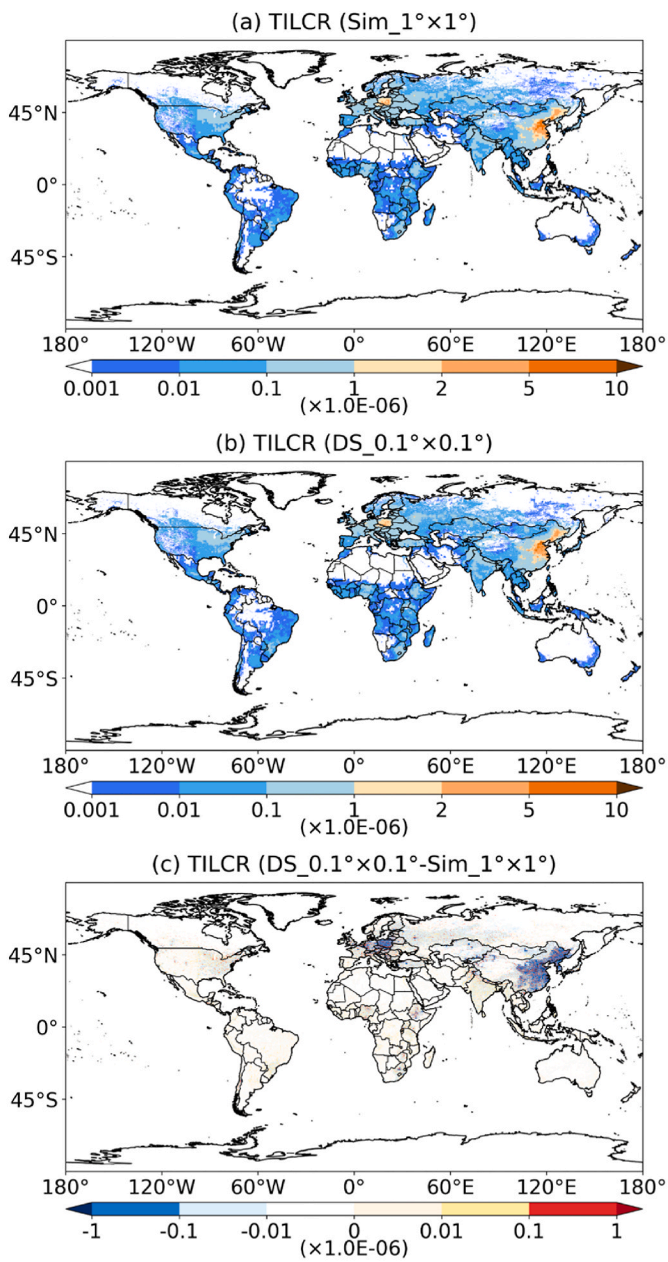

Fig. 7. Spatial distributions of TILCR (sum of ILCR of the two exposure paths) at $1^\circ \times 1^\circ$ resolution (a) and $0.1^\circ \times 0.1^\circ$ resolution (b) in 2013 and their difference (c), positive values indicate that the downscaling results are higher than the low-resolution simulations, and negative values are the opposite.

generate high-resolution simulations. The correlation coefficients (R^2) are all above 0.53 and the slope (k) is approximately 1, indicating a significant spatial correlation between the high-resolution and downscaled results. In general, BaP concentrations are highest in winter and lowest in summer, which is influenced by both emission sources and meteorological conditions. The R^2 for winter in China and Europe are 0.67 and 0.53, respectively, indicating that the downscaled results effectively reproduce the distribution characteristics of BaP in winter, when the concentrations are higher.

3.2. Regional and global distribution of BaP in different resolutions

Fig. 5 shows the annual mean BaP concentrations from low-resolution simulation, high-resolution simulation, and downscaling calculation over the nested areas in China and Central Europe in 2013. We find that the downscaling results show good agreement with the high-resolution simulations, in which the detailed features of hot spots are better captured than in low-resolution simulations. The distribution of BaP in the eastern provinces of China shows a higher concentration than in the western provinces (Fig. 5a) due to the higher emission, which is also found in other studies (Lou et al., 2023; Shrivastava et al., 2017). The highest BaP concentrations are found in Beijing-Tianjin-Hebei (BTH), Shandong, Henan, and the Yangtze River Delta (YRD), greatly higher than the European Union target value for BaP (1 ng m^{-3}). The above features are well characterized in high-resolution simulation (Fig. 5b) and downscaling results (Fig. 5c).

The downscaling result shows a slightly decreasing trend in most regions of China compared to the low-resolution results, except in some high-concentration areas, i.e. Beijing and Shanghai (Fig. 5e). At the high-concentration site in Beijing, the downscaling concentrations increased by about 11 ng m^{-3} compared to the low-resolution concentration, while the concentration around this site decreased with different levels. It can be seen that the concentrations at heavily polluted sites are underestimated when the resolution is coarse, while surrounding sites with low concentrations are also overestimated at the same time.

To verify the applicability of the methodology in different regions, a similar comparison was performed in Europe. Clearly, the downscaling approach reproduced the BaP concentration in Europe successfully. We found that all three results have high concentrations in the central areas (Fig. 5f, g, and h). Especially, Poland exhibits a large area of high concentrations (>2 ng m^{-3}) at high resolution. Although the area of high concentrations in Poland in the low-resolution and downscaled results became smaller than in the high-resolution simulations, it is still high (>1 ng m^{-3}) compared to other countries in Central Europe. This indicates a regional pollution of BaP in Poland. In addition, to validate the downscaling method across different years, we also compared the simulation and downscaling results for the annual mean BaP concentrations in 2018 (Fig. S1), and the key features of spatial variation are also reproduced.

The above results give us the confidence to use the downscaling method to improve the global map of BaP concentration based on coarse-resolution simulation. Fig. 6 shows the global spatial distributions of the annual mean BaP concentrations at $0.1^\circ \times 0.1^\circ$ resolution and the changes between the values at $1^\circ \times 1^\circ$ resolution and $0.1^\circ \times 0.1^\circ$ resolution in 2013 (a/b) and 2018 (c/d). The downscaling method is implemented based on the relative emissions (RAE) between coarse and fine resolution. As can be seen in Fig. 6b and d, the downscaled concentrations in Europe and China are lower than the low-resolution simulations, consistent with the trend in Fig. 2. In contrast, most regions such as the United States and Africa have higher downscaled concentrations. In summary, the downscaling results can capture more subtle localized features by obtaining higher-resolution spatial distributions while maintaining the low-resolution spatial distribution features. The key point is that the downscaling method can generate datasets in a way that saves a significant number of resources and time compared to direct high-resolution simulations with the model, which is crucial for global studies of PAHs.

3.3. Global health risks of PAHs

According to the USEPA (1991), $ILCR \leq 1 \times 10^{-6}$ indicates that the cancer risk is at an acceptable level, $1 \times 10^{-6} < ILCR \leq 1 \times 10^{-4}$ indicates that the cancer risk exceeds the acceptable level and there is a potential cancer risk, and $ILCR > 1 \times 10^{-4}$ indicates that the cancer risk is at an unacceptable level. Fig. 7a and b show the spatial distributions of TILCR (sum of ILCR through inhalation and dermal contact routes) in 2013 at $1^\circ \times 1^\circ$ and $0.1^\circ \times 0.1^\circ$ resolution, respectively. They have similar spatial distribution characteristics, e.g. both have large areas of TILCR $>1 \times 10^{-6}$ in eastern China and central Europe, indicating potential cancer risks in these areas. Compared to the spatial distributions of TILCR (Fig. 7c), we found that differences in most regions were within 1

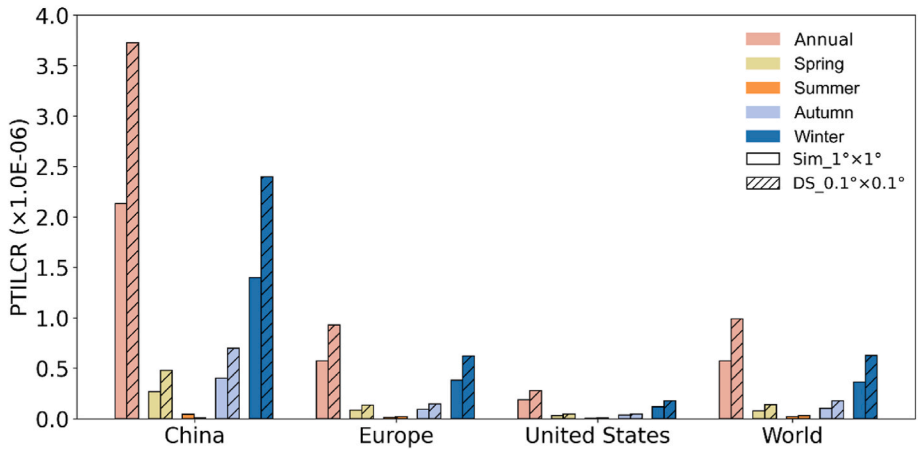

Fig. 8. The PTILCR in China, Europe, United States, and the world at 1° × 1° resolution and 0.1° × 0.1° resolution in 2013.

$\times 10^{-7}$, except for Central Europe and Eastern China, where the TILCR mainly showed a decreasing trend (with the greatest reduction of 3 $\times 10^{-6}$). The distribution characteristics in 2018 (Fig. S2) are similar to those in 2013, which are mainly related to changes in concentration (Fig. 6).

The population-weighted TILCR (PTILCR) across different seasons in 2013 is shown in Fig. 8. We found that the global PTILCR in 2013 was increased by 73.0 % from 5.7 $\times 10^{-7}$ in the 1° × 1° simulation to 1.0 $\times 10^{-6}$ in the 0.1° × 0.1° simulation. Among the regions, China has the largest PTILCR, which is consistent with the results of Shrivastava et al. (2017). This is significantly associated with the high emissions over densely populated areas. Especially, the high-resolution based PTILCR was increased significantly in China, from 2.1 $\times 10^{-6}$ to 3.7 $\times 10^{-6}$ (increased by 74.6 %) in 2013, and from 1.4 $\times 10^{-6}$ to 2.4 $\times 10^{-6}$ (increased by 71.4 %) in winter. This suggests that resolution is particularly critical in areas with dense populations and high emissions. The PTILCR in Europe increased from 3.8 $\times 10^{-7}$ to 6.2 $\times 10^{-7}$ (increased by 63.0 %) in winter and from 5.7 $\times 10^{-7}$ to 9.3 $\times 10^{-7}$ in 2013 (increased by 62.2 %). Although the PTILCR in the United States is lower than in China and Europe, it still increased from 1.9 $\times 10^{-7}$ to 2.8 $\times 10^{-7}$ in 2013. Clearly, high-resolution concentrations can significantly improve the accuracy and reliability of health risk assessments by resolving hotspots within an area of concern. Compared to 2013, the global PTILCR in 2018 (Fig. S3) decreased by 5.4 % and 7.8 % at low resolution and downscaled results, respectively. In China, the PTILCR in 2018 decreased by 6.5 % and 9.5 %, respectively, which is associated with emission reductions due to the implementation of "the Action Plan on Air Pollution Prevention and Control" in 2013.

We analyzed the cumulative probability distributions for the six age groups across four seasons in 2013 at 1° × 1° and 0.1° × 0.1° resolution (Fig. 9). The distribution in 2018 is shown in Fig. S4. The results indicate that the median estimated TILCR ranged from 1.76 $\times 10^{-7}$–1.14 $\times 10^{-6}$ for different age groups in 2013 (Fig. 9a). The order of TILCR from largest to smallest is: winter (1.12 $\times 10^{-7}$–7.19 $\times 10^{-7}$), autumn (3.13 $\times 10^{-8}$~2.07 $\times 10^{-7}$), spring (2.45 $\times 10^{-8}$~1.58 $\times 10^{-7}$), and summer (5.44 $\times 10^{-9}$~3.50 $\times 10^{-8}$). The TILCR shows a significant seasonal characteristic, which is closely associated with solid fuel combustion activities in winter. In the same season at the same resolution, children and young adults are the most sensitive group exposure to PAHs in atmosphere, which is consistent with the previous research by Ma et al. (2020). This may be related to the fact that young adults have longer exposure periods, faster inhalation rates, and more skin-exposed surfaces than other age groups. For children, this may be due to their high ratio of skin contact area to body weight and the higher frequency of hand contact with pollutants during outdoor activities. This result highlights the importance of considering age-specific exposure factors in risk assessment. For the whole year, the TILCR in 2013 was larger than 1 $\times 10^{-6}$ at the 92nd, 94th, and 99th percentile for children, adolescents, and young adults based on the low-resolution results, respectively. In the high-resolution result, the TILCR was larger than 1 $\times 10^{-6}$ at the 33rd, 61st, and 49th percentile for the above three groups, respectively. The distribution indicates that more people were exposed to potential health risks in the high-resolution result. These results further show that low-resolution simulations would likely underestimate the health risk. At the same resolution, the TILCR in 2018 was larger than 1 $\times 10^{-6}$ at the 44th, 68th, and 65th percentile for the above three groups, respectively, indicating that the health risk was decreased in 2018. We also analyzed the probability distribution of the higher-risk adult group across the four seasons at different resolutions, which further confirmed the importance of resolution in health risk assessment and the development of scientific management strategies.

3.4. Uncertainty analysis

A Monte Carlo simulation sensitivity analysis was conducted to evaluate the parameters in the exposure pathways (IR: inhalation rate; BW: body weight; SA: skin exposed surface area) that had the greatest impact on the calculation of the TILCR in six age groups. As shown in Fig. 10, there are significant differences in variance contributions among the various age groups. BW is the parameter that contributed the most to the TILCR, contributing 58.7 % and 66.7 % for children and adolescents, respectively, and even more than 85 % for young and middle-aged adults. SA contributed the next most to the TILCR, followed by IR. It is worth noting that the contribution of SA to children and adolescents is more significant than that to adults. This is because of the relatively high ratio of skin surface area to body weight in children and adolescents that leads to a more prominent role of dermal contact pathway in the health risks assessment. The Monte Carlo simulation analysis suggested that we could reduce the uncertainty of the estimated ILCR by improving the accuracy of these parameters.

4. Conclusions and discussion

In this paper, the global health risks of BaP are assessed based on high-resolution modeling by simulation and downscaling. This downscaling approach is based on the relative anthropogenic emissions and observations of BaP, providing high-resolution BaP concentrations and achieving a good compromise between data quality and computation cost. The high-resolution data of BaP can well reproduce the global distribution feature. The downscaling generally makes the simulated concentrations closer to the observations although the performance differs in different regions. By downscaling, PF2, PF5, and $\overline{S/O}$ increased from 33 % to 43 %, 76 % to 83 %, 0.43 to 1.12, and NMB decreased from

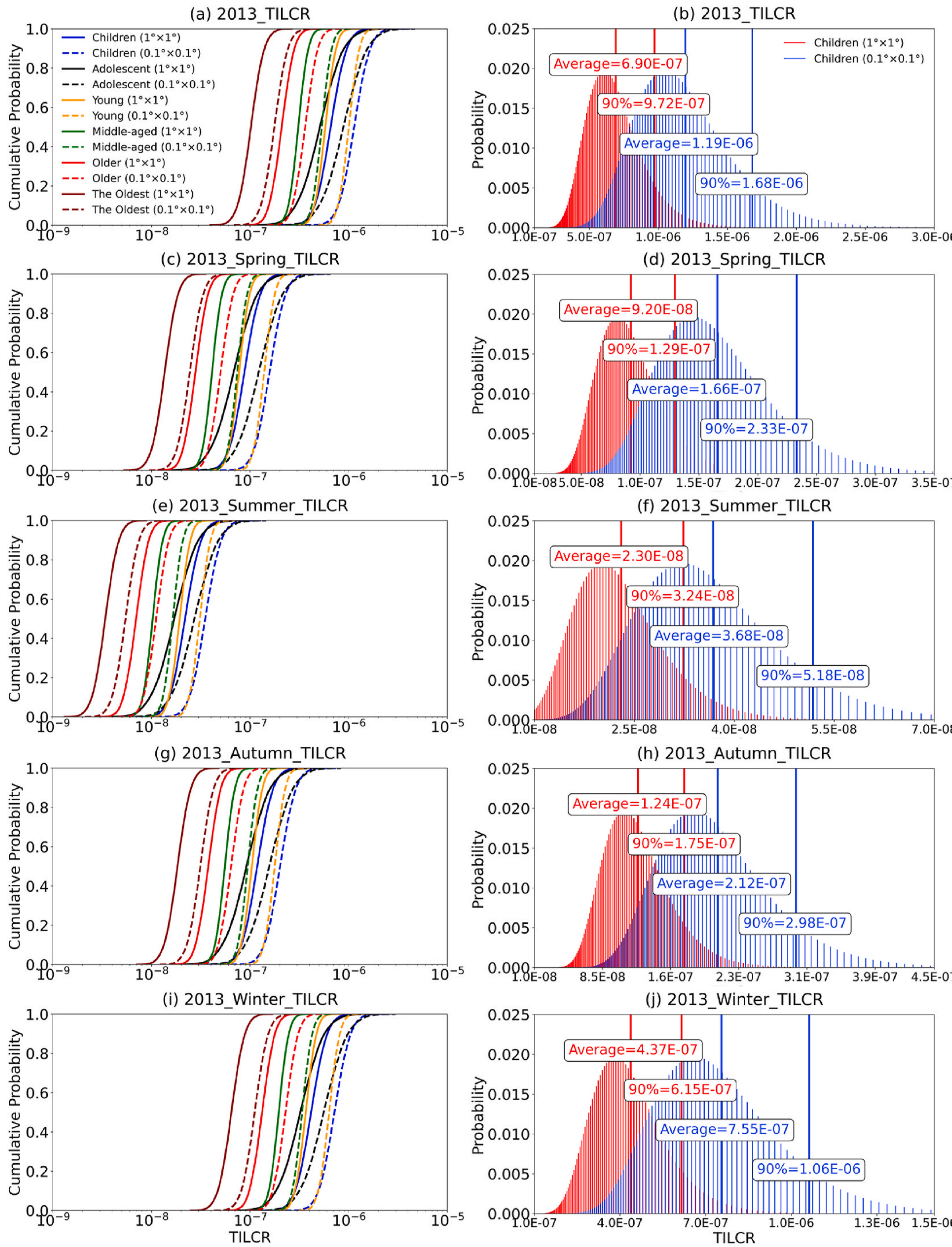

Fig. 9. The cumulative probabilities (a/c/e/g/i) of TILCR for children (blue), adolescents (black), young adults (orange), middle-aged adults (green), older adults (red), and the oldest adults (brown) and the probability (b/d/f/h/j) for children across four seasons and in 2013 at 1° × 1° and 0.1° × 0.1° resolution. (For interpretation of the references to colour in this figure legend, the reader is referred to the Web version of this article.)

−0.75 to −0.30, respectively. The high-resolution distribution of global BaP can be reliably used to assess health effects. The dataset makes up for the scarcity of observational data. The increased health risk revealed by the high-resolution data, with the global PTILCR increasing from 5.7 $\times$ 10^{-7} to 1.0 $\times$ 10^{-6}, indicates the necessity of using high-resolution data to evaluate the health risk posed by BaP and other PAHs. The order of age-specificity PTILCR from largest to smallest was: children, young adults, adolescents, and seniors, which may be related to the higher exposure in children and adults, suggesting that there is a need to consider the exposure characteristics of different populations when assessing the health risks. The PTILCR is highest in winter indicating the need to control solid fuel combustion activities and thereby reduce health risks. The results could provide an important guide for the development of scientific management strategies for different age groups, as well as for effective control policies to reduce health risks.

However, our study still has some uncertainties. Firstly, the high-resolution simulation by downscaling depends heavily on the observations and therefore the spatial and temporal representativeness of the collected observations is a major uncertainty, even though the spatial distribution of BaP concentrations has been well captured. More constraints of observation and using other downscaling methods such as machine learning (random forest and neural networks, etc.) would help

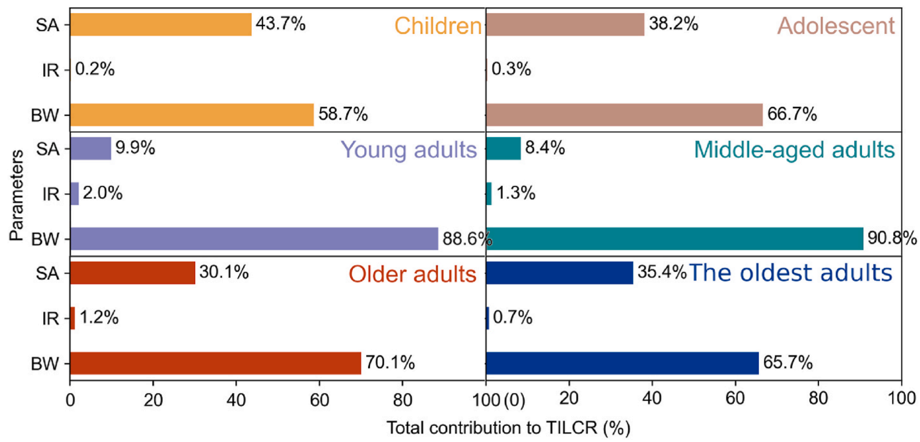

Fig. 10. Sensitivity analysis of TILCR in six age groups at 0.1° × 0.1° resolution.

decrease the uncertainties. Secondly, there remains uncertainty in the selected parameters for health risk assessment. In addition to body weight, inhalation rate, and surface area, there is uncertainty in other parameters such as the cancer slope factor. We did not adequately consider the impact of racial differences between the population. Thirdly, the health risk assessment method in this paper does not account for individual sensitivity differences and the dynamic cumulative effects of life-cycle exposure doses within the population.

In the future, we hope to obtain more observational data in developing countries to constrain the downscaling results, thus reducing uncertainty and enhancing the performance of the downscaling methods. In addition, we plan to use different downscaling methods to refine the multi-year PAH datasets with a wider variety of species for health risk assessment. We will introduce a well-defined Developmental Vulnerability Factor (DVF) and dynamic cumulative effects for the age groups considered, which will improve health risk assessment and provide a more realistic picture of the impact of PAHs.

CRediT authorship contribution statement

Zichen Wu: Writing – original draft, Visualization, Formal analysis. **Xueshun Chen:** Writing – review & editing, Supervision, Conceptualization. **Yuanlin Wang:** Writing – review & editing, Conceptualization. **Wenyi Yang:** Writing – review & editing. **Yang Wang:** Visualization, Software, Formal analysis. **Zhe Wang:** Writing – review & editing. **Huansheng Chen:** Writing – review & editing. **Lianfang Wei:** Writing – review & editing. **Wending Wang:** Data curation. **Huiyun Du:** Writing – review & editing. **Zhuoran Wang:** Visualization. **Ying Wei:** Writing – review & editing. **Xiao Tang:** Writing – review & editing. **Jie Li:** Writing – review & editing. **Lin Wu:** Writing – review & editing. **Zifa Wang:** Writing – review & editing, Supervision, Conceptualization.

Declaration of competing interest

The authors declare that they have no known competing financial interests or personal relationships that could have appeared to influence the work reported in this paper.

Acknowledgements

This research has been supported by the National Key R&D Program of China (2024YFC3711700) and the National Natural Science Foundation of China (Grant NO. 42377105 and 42305201). We also thank the National Key Scientific and Technological Infrastructure project "Earth System Science Numerical Simulator Facility" (EarthLab).

Appendix A. Supplementary data

Supplementary data to this article can be found online at https://doi.org/10.1016/j.atmosenv.2025.121340.

Data availability

The high-resolution dataset for monthly and annual averages of BaP concentrations in 2013 and 2018 has been submitted to Zendo (https://doi.org/10.5281/zenodo.13334701), with a data size of 1800 × 3600 (0.1° × 0.1°). The low-resolution dataset of BaP in 2013 and 2018 has been submitted to Zendo (https://doi.org/10.5281/zenodo.13334690), with a data size of 180 × 360 (1° × 1°).

References

Aunan, K., Ma, Q., Lund, M.T., Wang, S.X., 2018. Population-weighted exposure to PM2.5 pollution in China: an integrated approach. Environ. Int. 120, 111–120. https://doi.org/10.1016/j.envint.2018.07.042.

Boström, C.E., Gerde, P., Hanberg, A., Jernström, B., Johansson, C., Kyrklund, T., Rannug, A., Törnqvist, M., Victorin, K., Westerholm, R., 2002. Cancer risk assessment, indicators, and guidelines for polycyclic aromatic hydrocarbons in the ambient air. Environ. Health Perspect. 110, 451–488. https://doi.org/10.1289/ehp.02110s3451.

Byun, D., Schere, K.L., 2006. Review of the governing equations, computational algorithms, and other components of the models-3 Community Multiscale Air Quality (CMAQ) modeling system. Appl. Mech. Rev. 59 (1–6), 51–77. https://doi.org/10.1115/1.2128636.

Cao, X., Huo, S., Zhang, H., Zhao, X., Pang, C., Ma, C., Zheng, J., Wu, F., 2022. Intensive land-based activities increase the potential risk of benzo[α]pyrene (BaP) to aquatic ecosystems and human health in coastal areas of China. J. Clean. Prod. 371. https://doi.org/10.1016/j.jclepro.2022.133571.

Chang, K.F., Fang, G.C., Chen, J.C., Wu, Y.S., 2006. Atmospheric polycyclic aromatic hydrocarbons (PAHs) in Asia: a review from 1999 to 2004. Environ. Pollut. 142 (3), 388–396. https://doi.org/10.1016/j.envpol.2005.09.025.

Chen, H.S., Wang, Z.F., Li, J., Tang, X., Ge, B.Z., Wu, X.L., Wild, O., Carmichael, G.R., 2015. GNAQPMS-Hg v1.0, a global nested atmospheric mercury transport model: model description, evaluation and application to trans-boundary transport of Chinese anthropogenic emissions. Geosci. Model Dev. Discuss. (GMDD) 8 (9), 2857–2876. https://doi.org/10.5194/gmd-8-2857-2015.

Chen, S.C., Liao, C.M., 2006. Health risk assessment on human exposed to environmental polycyclic aromatic hydrocarbons pollution sources. Sci. Total Environ. 366 (1), 112–123. https://doi.org/10.1016/j.scitotenv.2005.08.047.

Chen, X.S., Yang, W.Y., Wang, Z.F., Li, J., Hu, M., An, J.L., Wu, Q.Z., Wang, Z., Chen, H.S., Wei, Y., Du, H.Y., Wang, D.W., 2019. Improving new particle formation simulation by coupling a volatility-basis set (VBS) organic aerosol module in NAQPMS plus APM. Atmos. Environ. 204, 1–11. https://doi.org/10.1016/j.atmosenv.2019.01.053.

Chen, X.S., Yu, F.Q., Yang, W.Y., Sun, Y.L., Chen, H.S., Du, W., Zhao, J., Wei, Y., Wei, L.F., Du, H.Y., Wang, Z., Wu, Q.Z., Li, J., An, J.L., Wang, Z.F., 2021. Global-regional nested simulation of particle number concentration by combing microphysical processes with an evolving organic aerosol module. Atmos. Chem. Phys. 21 (12), 9343–9366. https://doi.org/10.5194/acp-21-9343-2021.

Crippa, M., Solazzo, E., Huang, G.L., Guizzardi, D., Koffi, E., Muntean, M., Schieberle, C., Friedrich, R., Janssens-Maenhout, G., 2020. High resolution temporal profiles in the

emissions Database for global atmospheric research. Sci. Data 7 (1), 17. https://doi.org/10.1038/s41597-020-0462-2.
Dinkelacker, B.T., Rivera, P.G., Marshall, J.D., Adams, P.J., Pandis, S.N., 2023. High-resolution downscaling of source resolved PM2.5 predictions using machine learning models. Atmos. Environ. 310, 10. https://doi.org/10.1016/j.atmosenv.2023.119967.
Du, H.Y., Li, J., Chen, X.S., Wang, Z.F., Sun, Y.L., Fu, P.Q., Li, J.J., Gao, J., Wei, Y., 2019. Modeling of aerosol property evolution during winter haze episodes over a megacity cluster in northern China: roles of regional transport and heterogeneous reactions of SO2. Atmos. Chem. Phys. 19 (14), 9351–9370. https://doi.org/10.5194/acp-19-9351-2019.
Duan, X.L., Zhao, X.G., Chen, Y.T., Wang, B.B., Huang, N., Cao, S.Z., Dong, T., 2015. Highlights of the Chinese Exposure Factors Handbook (Adults). Science Press Beijing.
Duan, X.L., Zhao, X.G., Wang, B.B., Zhao, L.Y., Cheng, H.G., Cao, S.Z., 2016. Highlights of the Chinese exposure factors handbook. Children. China Environment Publishing Group.
Fang, B., Zhang, L., Zeng, H., Liu, J.J., Yang, Z., Wang, H.W., Wang, Q., Wang, M.M., 2020. $PM_{2.5}$-Bound polycyclic aromatic hydrocarbons: sources and health risk during non-heating and heating periods (tangshan, China). Int. J. Environ. Res. Publ. Health 17 (2), 16. https://doi.org/10.3390/ijerph17020483.
Friedman, C.L., Zhang, Y.X., Selin, N.E., 2014. Climate change and emissions impacts on atmospheric PAH transport to the arctic. Environ. Sci. Technol. 48 (1), 429–437. https://doi.org/10.1021/es403098w.
Fu, J.F., Ji, J.J., Luo, L., Li, X.H., Zhuang, X.X., Ma, Y., Wen, Q.L., Zhu, Y., Ma, J.J., Huang, J.Y., Zhang, D., Lu, S.Y., 2023. Temporal and spatial distributions, source identification, and health risk assessment of polycyclic aromatic hydrocarbons in PM2.5 from 2016 to 2021 in Shenzhen, China. Environ. Sci. Pollut. Res. 30 (47), 103788–103800. https://doi.org/10.1007/s11356-023-29686-0.
Hussain, M., Rae, J., Gilman, A., Kauss, P., 1998. Lifetime health risk assessment from exposure of recreational users to polycyclic aromatic hydrocarbons. Arch. Environ. Contam. Toxicol. 35 (3), 527–531. https://doi.org/10.1007/s002449900412.
Jury, W.A., Spencer, W.F., Farmer, W.J., 1983. Behavior assessment model for trace organics in soil: I. Model description. J. Environ. Qual. 12 (4), 558–564. https://doi.org/10.2134/jeq1983.00472425001200040025x.
Kohl, M., Lelieveld, J., Chowdhury, S., Ehrhart, S., Sharma, D., Cheng, Y.F., Tripathi, S. N., Sebastian, M., Pandithurai, G., Wang, H.L., Pozzer, A., 2023. Numerical simulation and evaluation of global ultrafine particle concentrations at the Earth's surface. Atmos. Chem. Phys. 23 (20), 13191–13215. https://doi.org/10.5194/acp-23-13191-2023.
Lammel, G., Dvorská, A., Klánová, J., Kohoutek, J., Kukacka, P., Prokes, R., Sehili, A.M., 2015. Long-range atmospheric transport of polycyclic aromatic hydrocarbons is worldwide problem - results from measurements at remote sites and modelling. Acta Chim. Slov. 62 (3), 729–735.
Lammel, G., Sehili, A.M., Bond, T.C., Feichter, J., Grassl, H., 2009. Gas/particle partitioning and global distribution of polycyclic aromatic hydrocarbons–a modelling approach. Chemosphere 76 (1), 98–106. https://doi.org/10.1016/j.chemosphere.2009.02.017.
Li, J., Wang, Z.F., Zhuang, G., Luo, G., Sun, Y., Wang, Q., 2012. Mixing of Asian mineral dust with anthropogenic pollutants over East Asia: a model case study of a super-duststorm in March 2010. Atmos. Chem. Phys. 12 (16), 7591–7607. https://doi.org/10.5194/acp-12-7591-2012.
Li, B.J., Lin, Y.Z., Wang, T., Jiang, W.Y.H., Wang, X.R., 2023. Atmospheric benzo a pyrene in the Yangtze River Delta, China: pollution level and lung cancer risk in 2016 and future predictions. Environ. Geochem. Health 45 (7), 4719–4735. https://doi.org/10.1007/s10653-023-01529-4.
Liao, K.Z., Yu, J.Z., 2020. Abundance and sources of benzo[a] pyrene and other PAHs in ambient air in Hong Kong: a review of 20-year measurements (1997-2016). Chemosphere 259, 9. https://doi.org/10.1016/j.chemosphere.2020.127518.
Lou, S.J., Shrivastava, M., Ding, A.J., Easter, R.C., Fast, J.D., Rasch, P.J., Shen, H.Z., Simonich, S.M., Smith, S.J., Tao, S., Zelenyuk, A., 2023. Shift in peaks of PAH-associated health risks from East Asia to south Asia and Africa in the future. Earth Future 11 (6), 15. https://doi.org/10.1029/2022ef003185.
Ma, W.L., Liu, L.Y., Jia, H.L., Yang, M., Li, Y.F., 2018. PAHs in Chinese atmosphere Part I: concentration, source and temperature dependence. Atmos. Environ. 173, 330–337. https://doi.org/10.1016/j.atmosenv.2017.11.029.
Ma, W.L., Zhu, F.J., Liu, L.Y., Jia, H.L., Yang, M., Li, Y.F., 2020. PAHs in Chinese atmosphere Part II: health risk assessment. Ecotoxicol. Environ. Saf. 200, 9. https://doi.org/10.1016/j.ecoenv.2020.110774.
Marusenko, Y., Herckes, P., Hall, S.J., 2011. Distribution of polycyclic aromatic hydrocarbons in soils of an arid urban ecosystem. Water Air Soil Pollut. 219 (1–4), 473–487. https://doi.org/10.1007/s11270-010-0721-5.
Mu, Q., Shiraiwa, M., Octaviani, M., Ma, N., Ding, A.J., Su, H., Lammel, G., Pöschl, U., Cheng, Y.F., 2018. Temperature effect on phase state and reactivity controls atmospheric multiphase chemistry and transport of PAHs. Sci. Adv. 4 (3), 8. https://doi.org/10.1126/sciadv.aap7314.
Octaviani, M., Tost, H., Lammel, G., 2019. Global simulation of semivolatile organic compounds - development and evaluation of the MESSy submodel SVOC (v1.0). Geosci. Model Dev. Discuss. (GMDD) 12 (8), 3585–3607. https://doi.org/10.5194/gmd-12-3585-2019.
Ravindra, K., Sokhi, R., Van Grieken, R., 2008. Atmospheric polycyclic aromatic hydrocarbons: source attribution, emission factors and regulation. Atmos. Environ. 42 (13), 2895–2921. https://doi.org/10.1016/j.atmosenv.2007.12.010.
Rivera, P.G., Dinkelacker, B.T., Kioutsioukis, I., Adams, P.J., Pandis, S.N., 2022. Source-resolved variability of fine particulate matter and human exposure in an urban area. Atmos. Chem. Phys. 22 (3), 2011–2027. https://doi.org/10.5194/acp-22-2011-2022.
Shen, H.Z., Tao, S., Liu, J.F., Huang, Y., Chen, H., Li, W., Zhang, Y.Y., Chen, Y.C., Su, S., Lin, N., Xu, Y.Y., Li, B.G., Wang, X.L., Liu, W.X., 2014. Global lung cancer risk from PAH exposure highly depends on emission sources and individual susceptibility. Sci. Rep. 4, 8. https://doi.org/10.1038/srep06561.
Shrivastava, M., Lou, S., Zelenyuk, A., Easter, R.C., Corley, R.A., Thrall, B.D., Rasch, P.J., Fast, J.D., Simonich, S.L.M., Shen, H.Z., Tao, S., 2017. Global long-range transport and lung cancer risk from polycyclic aromatic hydrocarbons shielded by coatings of organic aerosol. Proc. Natl. Acad. Sci. USA. 114 (6), 1246–1251. https://doi.org/10.1073/pnas.1618475114.
Skamarock, W.C., Klemp, J.B., Dudhia, J., Gill, D., Barker, D.M., Duda, M.G., Huang, X.-Y., Wang, W., Powers, J.G., 2008. A Description of the Advanced Research WRF Version 3.
Strand, A., Hov, O., 1996. A model strategy for the simulation of chlorinated hydrocarbon distributions in the global environment. Water Air Soil Pollut. 86 (1–4), 283–316. https://doi.org/10.1007/bf00279163.
Ting, Y.C., Ku, C.H., Zou, Y.X., Chi, K.H., Soo, J.C., Hsu, C.Y., Chen, Y.C., 2023. Characteristics and source-specific health risks of ambient PM2.5-bound PAHs in an urban city of northern Taiwan. Aerosol Air Qual. Res. 23 (11), 22. https://doi.org/10.4209/aaqr.230092.
USEPA, 1991. Risk assessment guidance for superfund: Volume I - human health evaluation manual (part B, development of risk-based Premliminary remediation goals). U.S. Environmental Protection Agency, Washington, DC.
Wang, R., Tao, S., Balkanski, Y., Ciais, P., Boucher, O., Liu, J.F., Piao, S.L., Shen, H.Z., Vuolo, M.R., Valari, M., Chen, H., Chen, Y.C., Cozic, A., Huang, Y., Li, B.G., Li, W., Shen, G.F., Wang, B., Zhang, Y.Y., 2014. Exposure to ambient black carbon derived from a unique inventory and high-resolution model. Proc. Natl. Acad. Sci. USA. 111 (7), 2459–2463. https://doi.org/10.1073/pnas.1318763111.
Wang, Z.F., Maeda, T., Hayashi, M., Hsiao, L.F., Liu, K.Y., 2001. A nested air quality prediction modeling system for urban and regional scales: application for high-ozone episode in Taiwan. Water Air Soil Pollut. 130 (1–4), 391–396. https://doi.org/10.1023/a:1013833217916.
Wei, Y., Chen, X.S., Chen, H.S., Li, J., Wang, Z.F., Yang, W.Y., Ge, B.Z., Du, H.Y., Hao, J. Q., Wang, W., Li, J.J., Sun, Y.L., Huang, H.L., 2019. IAP-AACM v1.0: a global to regional evaluation of the atmospheric chemistry model in CAS-ESM. Atmos. Chem. Phys. 19 (12), 8269–8296. https://doi.org/10.5194/acp-19-8269-2019.
World Health Organization (WHO), 2000. Air Quality Guidelines for Europe. World Health Organization, Regional Office for Europe Copenhagen, Denmark.
Wu, Z.C., Chen, X.S., Wang, Z.F., Chen, H.S., Wang, Z., Mu, Q., Wu, L., Wang, W.D., Tang, X., Li, J., Li, Y., Wu, Q.Z., Wang, Y., Zou, Z.Y., Jiang, Z.J., 2024. Modeling of polycyclic aromatic hydrocarbons (PAHs) from global to regional scales: model development (IAP-AACM_PAH v1.0) and investigation of health risks in 2013 and 2018 in China. Geosci. Model Dev. Discuss. (GMDD) 17 (24), 8885–8907. https://doi.org/10.5194/gmd-17-8885-2024.
Xia, Z.H., Duan, X.L., Tao, S., Qiu, W.X., Liu, D., Wang, Y.L., Wei, S.Y., Wang, B., Jiang, Q.J., Lu, B., Song, Y.X., Hu, X.X., 2013. Pollution level, inhalation exposure and lung cancer risk of ambient atmospheric polycyclic aromatic hydrocarbons (PAHs) in Taiyuan, China. Environ. Pollut. 173, 150–156. https://doi.org/10.1016/j.envpol.2012.10.009.
Zhang, M., Xie, J.F., Wang, Z.T., Zhao, L.J., Zhang, H., Li, M., 2016. Determination and source identification of priority polycyclic aromatic hydrocarbons in PM2.5 in Taiyuan, China. Atmos. Res. 178, 401–414. https://doi.org/10.1016/j.atmosres.2016.04.005.
Zhang, P., Chen, Y., 2017. Polycyclic aromatic hydrocarbons contamination in surface soil of China: a review. Sci. Total Environ. 605–606, 1011–1020. https://doi.org/10.1016/j.scitotenv.2017.06.247.
Zhang, Y., Hemperly, J., Meskhidze, N., Skamarock, W.C., 2012. The global weather research and forecasting (GWRF) model: model evaluation, sensitivity study, and future year simulation. Atmos. Clim. Sci. 2, 231–253. https://doi.org/10.4236/acs.2012.23024.
Zhang, Y., Tao, S., Ma, J., Simonich, S., 2011. Transpacific transport of benzo[a]pyrene emitted from Asia. Atmos. Chem. Phys. 11 (23), 11993–12006. https://doi.org/10.5194/acp-11-11993-2011.
Zhang, Z., Yuan, Q., Wang, M., Hu, T., Huang, Y., Xiu, G., Lai, S., Gao, Y., Lee, S.C., 2023. Exposure and health risk assessment of PM2.5-bound polycyclic aromatic hydrocarbons during winter at residential homes: a case study in four Chinese cities. Sci. Total Environ. 895. https://doi.org/10.1016/j.scitotenv.2023.165111.
Zhu, Y., Tao, S., Price, O.R., Shen, H., Jones, K.C., Sweetman, A.J., 2015. Environmental distributions of benzo[a]pyrene in China: current and future emission reduction scenarios explored using a spatially explicit multimedia fate model. Environ. Sci. Technol. 49 (23), 13868–13877. https://doi.org/10.1021/acs.est.5b00474.